Title

Nuclear rupture at sites of high curvature compromises retention of DNA repair factors.

Journal

The Journal of cell biology, 217(11)

ISSN

0021-9525

Authors

Xia, Yuntao
Ivanovska, Irena L
Zhu, Kuangzheng
et al.

Publication Date

2018-11-01

DOI

10.1083/jcb.201711161

Peer reviewed

JCB Journal of Cell Biology

REPORT

Nuclear rupture at sites of high curvature compromises retention of DNA repair factors

Yuntao Xia[1,2*], Irena L. Ivanovska[1,2*], Kuangzheng Zhu[1,2], Lucas Smith[1,2], Jerome Irianto[1,2], Charlotte R. Pfeifer[1,2], Cory M. Alvey[1,2,3], Jiazheng Ji[1,2], Dazhen Liu[1,2], Sangkyun Cho[1,2], Rachel R. Bennett[1,3], Andrea J. Liu[1,3], Roger A. Greenberg[1,4], and Dennis E. Discher[1,2,3]

The nucleus is physically linked to the cytoskeleton, adhesions, and extracellular matrix—all of which sustain forces, but their relationships to DNA damage are obscure. We show that nuclear rupture with cytoplasmic mislocalization of multiple DNA repair factors correlates with high nuclear curvature imposed by an external probe or by cell attachment to either aligned collagen fibers or stiff matrix. Mislocalization is greatly enhanced by lamin A depletion, requires hours for nuclear reentry, and correlates with an increase in pan-nucleoplasmic foci of the DNA damage marker γH2AX. Excess DNA damage is rescued in ruptured nuclei by cooverexpression of multiple DNA repair factors as well as by soft matrix or inhibition of actomyosin tension. Increased contractility has the opposite effect, and stiff tumors with low lamin A indeed exhibit increased nuclear curvature, more frequent nuclear rupture, and excess DNA damage. Additional stresses likely play a role, but the data suggest high curvature promotes nuclear rupture, which compromises retention of DNA repair factors and favors sustained damage.

Introduction

Cytoskeletal forces applied to the ECM via adhesions are also exerted on the nucleus (Wang et al., 2009). Structural proteins generally sustain such forces up to the point at which some protein or its assembly breaks; even a microtubule well known for its rigidity bends and breaks under cytoskeletal forces (Odde et al., 1999). For the nucleus, lamin intermediate filament meshworks (Turgay et al., 2017) somehow stiffen the nucleus and sustain nuclear forces (Lammerding et al., 2007). Indeed, fibroblasts mutated or deficient in lamin A/C (lamin A hereafter) exhibit nuclear rupture with mislocalization of GFP–nuclear localization signal (NLS) constructs and GFP-tagged transcription factors, at least in sparse culture on standard rigid dishes (De Vos et al., 2011). Soft gels limit cell and nuclear spreading as well as stress fiber assembly (Swift et al., 2013; Buxboim et al., 2017), and soft gels rescue mislocalization of GFP-NLS, as does F-actin inhibition (Tamiello et al., 2013). Furthermore, an acetyl-transferase inhibitor that affects cytoskeleton assembly (Oh et al., 2017) also rescues highly curved nuclear shapes of lamin A mutants and excess DNA damage (Larrieu et al., 2014). Senescence/apoptosis that is often associated with DNA damage is additionally rescued by culturing mutant cells on almost any type of ECM rather than on rigid plastic (Hernandez et al., 2010; de la Rosa et al., 2013). Mechanisms of nuclear rupture and DNA damage nonetheless remain unclear.

DNA damage and repair are ongoing in the nucleus, with DNA repair factors diffusing to damage sites. DNA damage requires hours for repair to a basal level following acute exposure to damage-causing agents (Burma et al., 2001; Soubeyrand et al., 2010). However, multiple DNA repair factors (e.g., BRCA1) mislocalize to cytoplasm in breast tumors, and nuclear depletion associates with DNA damage and patient survival (Alshareeda et al., 2016). Breast tumors also have low lamin A (Capo-chichi et al., 2011), as do several other cancers (Broers et al., 1993; Kaspi et al., 2017). Mislocalization of DNA repair factors such as 53BP1 can lead to their progressive loss (Nuciforo et al., 2007), with cytoplasmic degradation of the DNA repair complex KU70–KU80 also suggested in senescence of nonmalignant cells on rigid plastic (Seluanov et al., 2007). Nuclear rupture is one conceivable mechanism for mislocalization of DNA repair factors and a consequent excess of DNA damage. We hypothesized that such a process occurs as a result of high nuclear curvature, with rupture frequency increased by both intracellular and extracellular structural factors that include low levels of lamin A, high actomyosin stress, and stiff ECM.

[1]Physical Sciences Oncology Center at Penn, University of Pennsylvania, Philadelphia, PA ; [2]Molecular and Cell Biophysics Lab, University of Pennsylvania, Philadelphia, PA; [3]Graduate Group, Department of Physics and Astronomy, University of Pennsylvania, Philadelphia, PA; [4]Cancer Biology, Abramson Family Cancer Research Institute, Perelman School of Medicine, University of Pennsylvania, Philadelphia, PA.

*Y. Xia and I.L. Ivanovska contributed equally to this paper; Correspondence to Dennis E. Discher: discher@seas.upenn.edu.

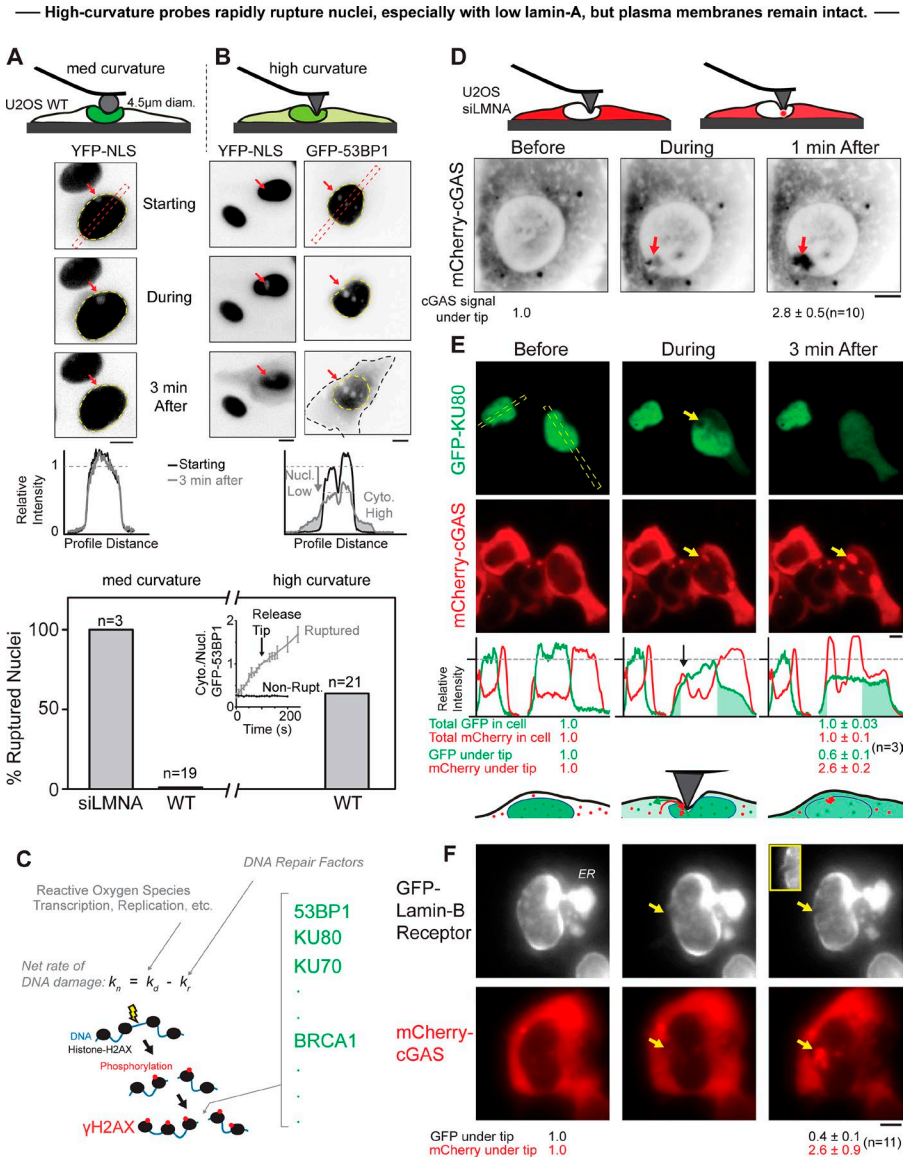

Figure 1. **High-curvature probes rapidly rupture nuclei without disrupting plasma membrane. (A)** Probing nuclei in living WT U2OS cells at constant force (~10–20 nN) with medium-curvature beads (diameter = 4.5 µm) shows no YFP-NLS mislocalization (inverse gray-scale), whereas lamin A knockdown (siLMNA) causes frequent mislocalization (bar graph). **(B)** High-curvature tips (diameter < 0.1 µm) rupture WT nuclei, based on mislocalization of YFP-NLS or GFP-53BP1 into cytoplasm within minutes (10/15 ruptured for GFP-53BP1 and 4/6 ruptured for YFP-NLS). Intensity profiles show decreased nuclear signal and higher cytoplasmic signal. Inset: Cytoplasmic GFP accumulates even after probe tip is removed. **(C)** Various DNA repair proteins may be affected when the nuclear envelope ruptures. **(D)** DNA binding protein cGAS (dark gray) enters the nucleus under a high-curvature tip. **(E)** DNA repair factor GFP-KU80 mislocalizes to cytoplasm simultaneously with cGAS accumulation under the probe tip. Total GFP and mCherry in the cell (bottom numbers) remain constant during the entire export, indicating plasma membrane integrity. **(F)** A gap in nuclear envelope GFP-LBR coincides spatiotemporally with cGAS accumulation under a probe tip, indicating nuclear envelope rupture. Bars, 10 µm. Arrows in A, B, and D–F point to site of AFM tip indentation of nucleus. All data are presented as mean ± SEM.

Results and discussion

High-curvature probes rapidly rupture nuclei without disrupting the plasma membrane

Nuclei in live U2OS osteosarcoma cells were probed with atomic force microscopy (AFM) tips of either medium or high curvature (4.5-µm sphere or pyramidal tip <0.1-µm diameter; Fig. 1, A and B). The force was held constant in a poly nano-Newton (nN) range similar to the contractile forces generated by cells (Saez et al., 2005). Nuclear factors that are known to be mobile within the nucleus were observed simultaneously with probing: these included YFP-NLS and GFP fusions of DNA repair factors 53BP1 and KU80 (Fig. 1 C). Sudden mislocalization to cytoplasm was frequently evident when probing with medium curvature tips after lamin A knockdown (Fig. S1 A), whereas WT nuclei required high-curvature tips (Fig. 1, A and B, bar graph). YFP or GFP signal filled the cytoplasm for minutes even after release of the AFM tip (Fig. 1 B, inset). The images suggest an intact plasma membrane and sustained selective rupture of the nuclear envelope; in contrast, changes in nuclear signal that reverse within seconds have been attributed to distortion of nuclear pores (Elosegui-Artola et al., 2017). Furthermore, lamin A is most abundant in stiff tissues such as bone (Swift et al., 2013), which is relevant to osteosarcoma, and our probing begins to suggest that lamin A protects against curvature-induced rupture.

Sites of nuclear rupture in interphase cells are marked by focal DNA binding of cytoplasmic cyclic GMP-AMP synthase (cGAS) upon cell migration through circular pores (Harding et al., 2017) or rectangular channels with high-curvature corners (Denais et al., 2016; Raab et al., 2016). Within nonmigrating cells probed in this study by AFM, mCherry-cGAS enriches within seconds where the tip indents the nucleus (Fig. 1 D), and the mobile DNA repair factor GFP-KU80 simultaneously mislocalizes to cytoplasm (Fig. 1 E). Neither cGAS nor the repair factor decrease significantly in total signal, which provides quantitative evidence of plasma membrane integrity (Fig. 1 E, bottom). Because cGAS might enter nuclear pores distorted under the AFM tip, we imaged lamin B receptor (LBR; GFP-LBR), which is an integral membrane protein that binds lamin B and mirrors rupture of

the lamin B meshwork after constricted migration (Buxboim et al., 2017). Under AFM tips, LBR gaps are evident at sites of cGAS nuclear entry (Fig. 1 F). LBR in ER and elsewhere was otherwise unaffected by high-curvature perturbations.

Collagen fiber films promote nuclear curvature and DNA repair factor mislocalization

To test the hypothesis that nuclear curvature generated by a cell—rather than by external probes, pores, or channels—accelerates nuclear rupture with mislocalization of key nuclear factors, lamin A–knockdown cells were cultured on nanofilms of collagen I fibers that align as they self-assemble on mica (Fig. 2 A; Ivanovska et al., 2017). The U2OS cells and their nuclei elongate along fibers (Figs. 2 B and S1 B), appearing similar to other mesenchyme-derived cells in tendons (Docheva et al., 2005). The nanofilms are soft only in the sense that adjacent fibers are visibly pulled off of the nonadhesive mica after 6–12 h of cell adhesion; this limits lateral spreading of a cell and thus favors a high aspect ratio (AR; Fig. 2 B). Past research of lamin A–defective fibroblasts on soft gel substrates would predict no nuclear rupture (Tamiello et al., 2013).

Immunostaining for DNA repair factor KU70 showed cytoplasmic mislocalization within cells with high-AR nuclei (Fig. 2 C). Normalized maximum curvature increases with AR (Fig. 2 D) but is lower than ellipse theory at high AR, which suggests the nucleus resists strong bending (at the poles). Circularity is more similar in experiment and theory because circularity is less sensitive to the local differences at nuclear poles. Mislocalization of GFP-KU70 accompanied enrichment of mCherry-cGAS at nuclear pole(s) (Fig. 2 E, images). Furthermore, if cGAS foci were seen in a nucleus, then the same cell showed high cytoplasmic GFP-KU70 (Fig. 2 E, bar graph). Because KU70 dimerizes with KU80, similar mislocalization phenomena are expected for both (e.g., Fig. 1 D). Nuclear curvature imposed by cell-generated forces (that are also resisted by stiff ECM) thus increases the likelihood of focal nuclear rupture. Cell and nuclear responses to stiff ECM along the fiber direction, rather than lateral softness, are consistent with cells responding to other anisotropic substrates such as rigid glass hidden below a thin soft gel (Buxboim et al., 2017).

Excess DNA damage in cells correlates with mislocalized DNA repair factors

Partial knockdown of lamin A with shLMNA was stably achieved in A549 lung carcinoma cells, whereas shLMNA-treated U2OS cells showed a growth defect (Fig. S1 C). These cells grew normally (Fig. S1 D), but ~10–20% of nuclei exhibited KU80 mislocalization in cells on rigid coverslips (Fig. S1 E). A relationship with nuclear curvature was evident (even without collagen fiber films): the lamina was disrupted at nuclear poles with enrichment of the residual lamin A and depletion of lamin B (Fig. 3 A, i and ii). Anticorrelated distributions of lamin A and B occur at sites of nuclear rupture (also at nuclear poles) during constricted migration (Harada et al., 2014; Denais et al., 2016). Ruptured A549 nuclei were also more elongated, with lower nuclear circularity compared with nonruptured nuclei, while nuclear area was constant (Fig. 3 A, iii).

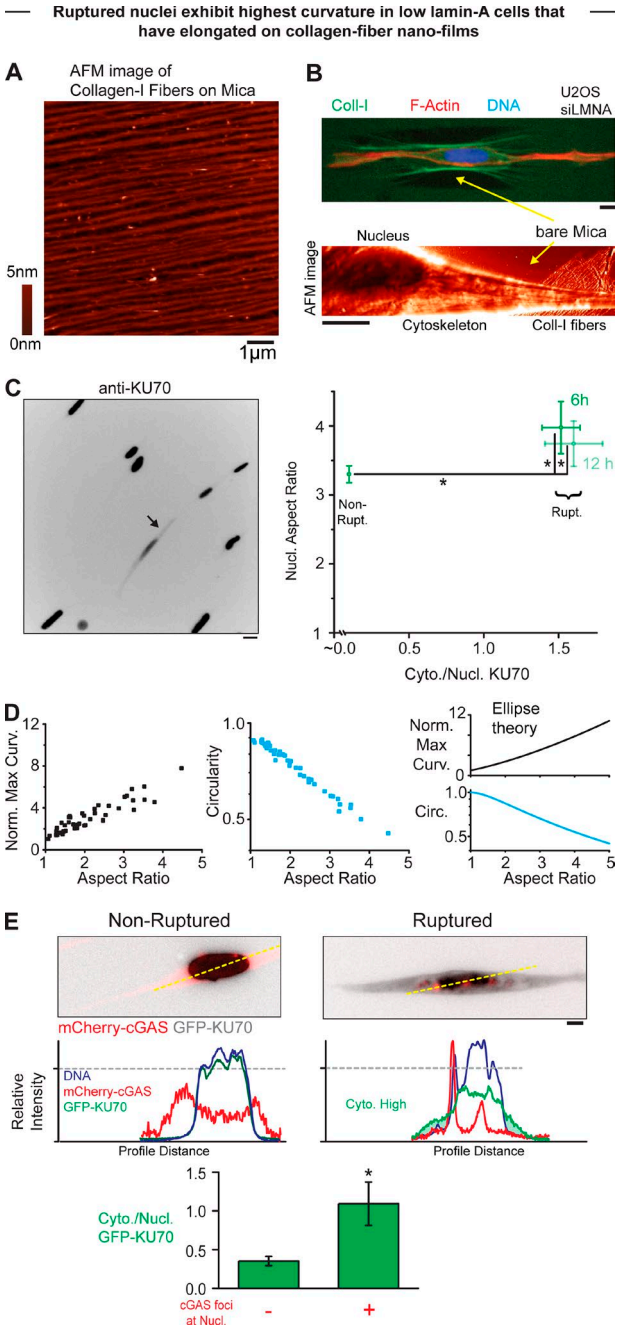

Figure 2. **Aligned collagen fiber film promotes nuclear curvature and DNA repair factor mislocalization. (A)** AFM image of long-range alignment of collagen fibrils. **(B)** Both immunofluorescence and AFM probing confirm cells elongate only along the collagen fibers. **(C)** Immunofluorescent image and quantitation of DNA repair factor KU70 in fixed cells after 6 h seeding. Ruptured nuclei (arrow in image) show high cytoplasmic/nuclear intensity ratio (plot) and are more elongated than nonruptured nuclei (low cytoplasmic/nuclear ratio) at 6 and 12 h. $n > 15$ cells per point in three experiments analyzing >100 cells per experiment. **(D)** As nuclear AR increases, normal maximum curvature Increases, and circularity decreases. Our model predicts the trend. $n = 46$. **(E)** In nonruptured nuclei, cGAS is cytoplasmic, but cGAS enriches at high-curvature sites of ruptured nuclei as validated by higher cytoplasmic/nuclear GFP-KU70 (bar graph). $n > 10$ cells. *, $P < 0.05$. Bars, 10 μm. All data are presented as mean ± SEM.

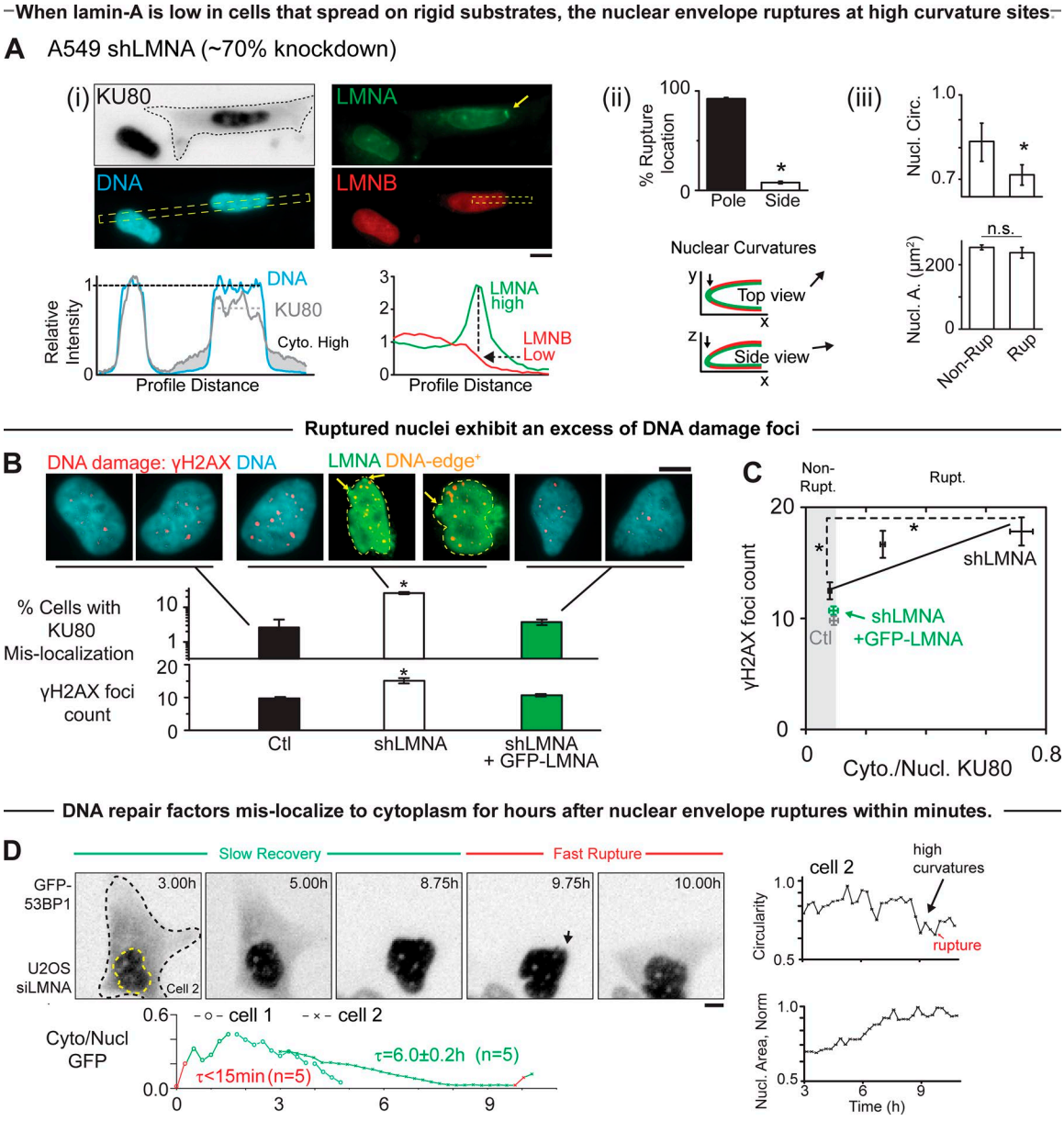

Figure 3. **Excess DNA damage in cells correlates with mislocalized DNA repair factors. (A)** i: Ruptured A549 shLMNA nuclei show high cytoplasmic KU80 by immunofluorescence; the lamina is focally enriched in lamin A (arrow) and depleted in lamin B. ii: 92% of rupture events occur at poles of nuclei where curvature is high. Cartoon shows 2D curvature in cells. iii: Ruptured nuclei have lower circularity, indicating high curvature. Overall nuclear area is the same. $n > 150$ cells in three experiments. **(B)** Lamin A knockdown increases the fraction of cells with mislocalized cytoplasmic KU80 and excess DNA damage as indicated by γH2AX foci. GFP-LMNA rescues both effects. γH2AX foci in nuclei of shLMNA cells are not enriched near lamina rupture sites (arrows). $n > 150$ cells in three experiments. **(C)** For shLMNA cells, ruptured nuclei with higher cytoplasmic/nuclear KU80 have higher γH2AX foci counts compared with nonruptured ones with low cytoplasmic/nuclear KU80. Ctl and GFP-LMNA–rescued cells rarely rupture and show low cytoplasmic/nuclear KU80 and low γH2AX foci counts. $n > 150$ cells in three experiments. *, $P < 0.05$. **(D)** Time-lapse imaging: Mislocalized cytoplasmic GFP-53BP1 recovers over hours into nuclei. Shape fluctuations of U2OS siLMNA nuclei create high-curvature regions (arrow) before second GFP-53BP1 mislocalization. Cytoplasmic/nuclear GFP is plotted over time ($n = 5$ cells). Right plots: Nuclear circularity and area over time. High curvature occurs <1 h before rupture. Bars, 10 µm. All data are present as mean ± SEM.

DNA repair and DNA damage are ongoing (Fig. 1 C), and cell growth checkpoints require low damage. Immunostaining for the DNA damage marker γH2AX (Darzynkiewicz et al., 2011) together with KU80 indeed shows KU80 mislocalization tends to correlate with excess γH2AX foci in the shLMNA cells (Fig.3, B and C). DNA damage foci were randomly distributed throughout the nucleoplasm rather than concentrated near sites of high-curvature lamina disruption (Fig. 3 B, images). Stable expression of GFP-LMNA rescued knockdown cells, and an electrophoretic comet assay for DNA damage confirmed the imaging (Fig. S1 F). Such a distribution is consistent with impeded repair of dispersed DNA damage.

Rescue of rupture-induced DNA damage by cooverexpression of DNA repair factors

Repair of DNA requires hours after acute damage by either radiation or drugs (Staszewski et al., 2008; Álvarez-Quilón et al., 2014). While GFP-NLS type constructs reenter nuclei quickly

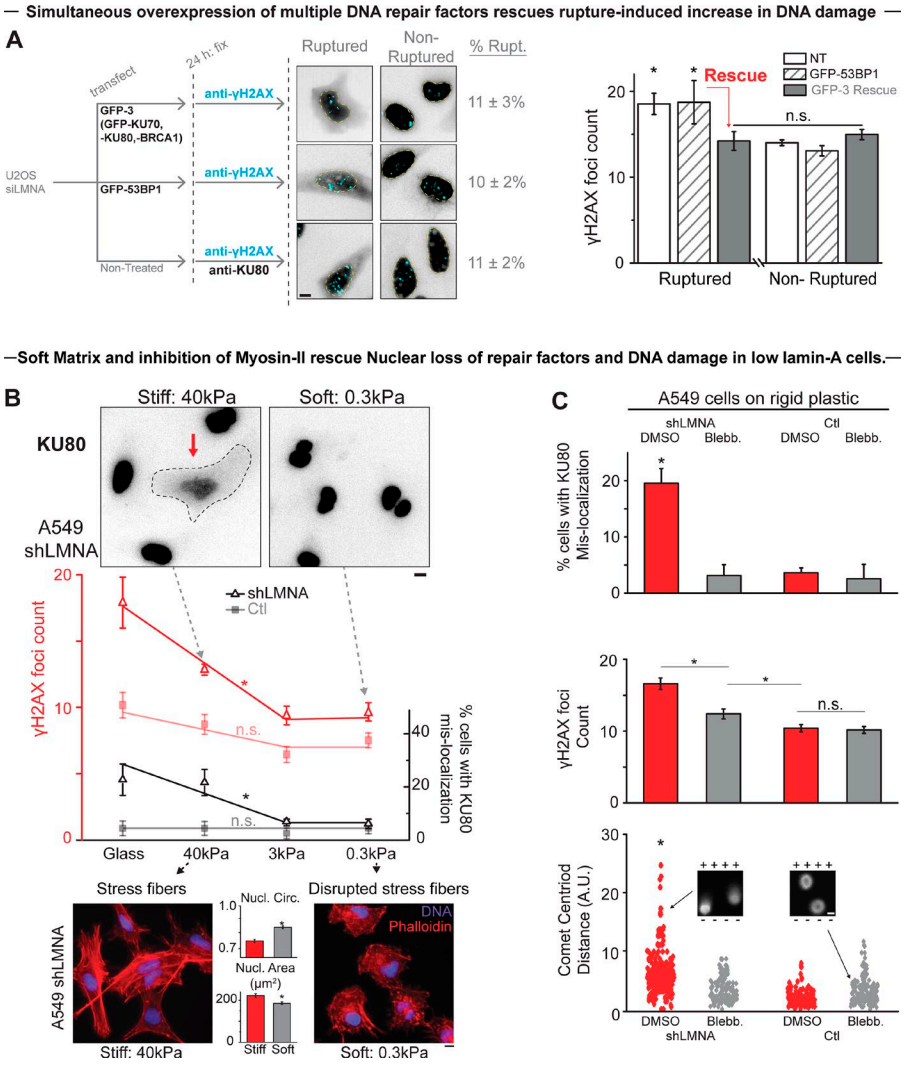

Figure 4. **Cooverexpression of multiple DNA repair factors, soft ECM, and myosin II inhibition rescue rupture-induced DNA damage in low–lamin A cells. (A)** siLMNA-U2OS cells were fixed after 24 h DNA repair factor transfection and immunostained for γH2AX. The nontransfected (NT) sample was also stained for KU80. Cytoplasmic mislocalization of the GFP or KU80 identifies ruptured nuclei. Bar graph: Cotransfection of DNA repair factors KU70, KU80, and BRCA1 (GFP-3) rescues excess DNA damage in ruptured nuclei, whereas ruptured nuclei with GFP-53BP1 (and NT) maintain excess DNA damage. Nonruptured cells always show a basal level of DNA damage. n = 30–100 cells per condition in three experiments. **(B)** Excess DNA damage and loss of repair factors in A549 shLMNA nuclei is suppressed by culturing on softer gels (3 or 0.3 kPa), whereas Ctl cells are unaffected. Bottom: Culturing A549 shLMNA cells on soft gels (0.3 kPa) leads to less stress fiber assembly in conjunction with rounder and smaller nuclei. n > 100 cells per condition in three experiments. **(C)** Nuclear envelope rupture and excess DNA damage (γH2AX foci counts and comet assay) in A549 shLMNA cells cultured on rigid plastic are reduced to Ctl levels after myosin II inhibition by blebbistatin, while Ctl cells are unaffected. n > 100 cells per condition in three experiments. *, $P < 0.05$. Bars, 10 µm. All data are present as mean ± SEM.

(<1 h) after nuclear rupture and resealing (Hatch and Hetzer, 2016; Raab et al., 2016), DNA repair factors appear mislocalized more frequently, suggesting slower relocalization (Fig. S1 G). GFP-NLS is far smaller than many repair factors (e.g., 53BP1, BRCA1, or KU80–KU70 heterodimers ∼150–250 kD), and even passive permeation through nuclear pores decreases strongly with molecular size (Samudram et al., 2016). To study the kinetics of GFP-53BP1 mislocalization, U2OS cells on rigid coverslips were imaged live for ∼10 h. Decreased nuclear circularity and increased cell spreading are seen before nuclear envelope rupture (Fig. 3 D, right), suggesting rupture at a high-curvature fluctuation in a tensed nucleus. Deep knockdown of lamin A increased rupture ∼5–10-fold (to ∼10%) in both live and fixed samples (Fig. S1 H), and nuclear rupture caused rapid mislocalization (<15 min) with slow recovery back into the nucleus (∼6 h; Fig. 3 D). GFP-53BP1 loss to cytoplasm was accompanied by simultaneous mislocalization of endogenous DNA repair factors upon immunostaining after live-cell imaging (KU80 in Fig. S1 I), with simultaneous mislocalization observed for all DNA repair factors examined (BRCA1, KU70, RPA2, and BRCA2 in Fig. S2 A).

If mislocalization of key repair factors shifts the steady state toward excess DNA damage (Fig. 1 C), then their simultaneous overexpression within ruptured nuclei should rescue damage. KU80 and KU70 form heterodimers and repair DNA damage in a pathway orthogonal to that of BRCA1 (Gudmundsdottir and Ashworth, 2006; Chang et al., 2017), and partial knockdown of each repair factor results in excess DNA damage that is specifically rescued by repair factor overexpression without affecting a basal damage (Fig. S2 B). Expression plasmids for these three repair factors were thus pooled for cooverexpression (denoted GFP-3) in U2OS lamin A–knockdown cells (Fig. S2 C). GFP-53BP1 was used as a negative control (Ctl) because neither its overexpression nor si53BP1 affect DNA damage (Fig. S2 D). Rupture was assessed by cytoplasmic mislocalization of endogenous DNA repair factors or GFP fusions, and the latter transfections did not alter the ∼10% of ruptured cells in fixed cultures (Fig. 4 A). Even with rupture, nuclear GFP signal was intense relative to antibody staining for repair factors. For ruptured nuclei with cytoplasmic KU80 or GFP-53BP1, DNA damage was in equal excess, but GFP-3 rescued excess damage (Fig. 4 A). For nonruptured nuclei, GFP-3 had no effect on basal DNA damage (Fig. 4 A), and so the

three DNA repair factors are not limiting except when the nucleus ruptures.

Rescue of nuclear rupture and DNA damage by soft ECM and myosin II inhibition

Since mislocalization of DNA repair factors results from nuclear envelope rupture that relates to curvature and forces on the nucleus, reduction of such nuclear stress should in principle rescue mislocalization of DNA repair factors and thereby rescue the excess DNA damage. Soft matrices minimize actomyosin contractility and cause cells and nuclei to be less spread with lower curvature and less lamin A (Swift et al., 2013; Buxboim et al., 2017) as confirmed for WT A549 (Fig. S2 E). A549 shLMNA cells on gels that are in the range of soft tissues (3 and 0.3 kPa; Swift et al., 2013) showed minimal nuclear rupture and DNA damage (Fig. 4 B) relative to cells on stiff gels (40 kPa mimics some fibrotic tissues; Dingal et al., 2015). Soft gels minimized actomyosin assembly and nuclear curvature as expected (Fig. 4 B, bar graph), and WT A549 cells showed little evidence of nuclear rupture or excess DNA damage.

Actomyosin tension drives spreading of a cell and its nucleus on rigid culture substrates, but myosin II relaxation by blebbistatin causes rapid cell and nuclear rounding (Fig. S2 F; Buxboim et al., 2014, 2017). Such inhibition again decreased cytoplasmic mislocalization of KU80 in shLMNA A549 cells to Ctl levels and also decreased DNA damage to levels similar to soft gels based on γH2AX foci and electrophoretic comet assays (Fig. 4 C). A small, persistent excess of DNA damage in knockdown cells after relaxing nuclear curvature (by soft ECM or myosin II inhibition) is consistent with partial loss of DNA repair factors in long-term, plastic-cultured shLMNA cells (BRCA1 and 53BP1, but not KU80; Fig. S2 G), although repair factor levels are unaffected by short-term perturbations (blebbistatin and gel cultures; Fig. S2, H and I). For 53BP1, protein degradation is faster in lamin A mutant cultures (Das et al., 2013); turnover could be favored by cytoplasmic mislocalization.

Overexpression of nonmuscle myosin II in WT cells with normal lamin A levels have the opposite effects of the above rescues. WT nuclei exhibited higher curvature, more cytoplasmic mislocalization of KU80, and more DNA damage by two assays (Fig. S3). Blebbistatin again rescued the effects. The results might explain why hyperactivation of nonmuscle myosin II (by depleting a repressive phosphatase) causes nuclear dysmorphia in standard cultures and increased DNA damage (Takaki et al., 2017). Lamin A defects are therefore unnecessary for nuclear disruption and DNA damage.

Solid tumors: High-curvature nuclei, mislocalized repair factors, and excess DNA damage

ECM stiffness can be high in solid tumors (Levental et al., 2009). We hypothesized that lamin A knockdown cells exhibit some of the processes in vivo as seen in cultures on rigid substrates. Lung tumors have low lamin A (Broers et al., 1993; Kaspi et al., 2017), and so lung-derived A549 Ctl and shLMNA cells expressing tdTomato were engrafted in mice (Fig. 5 A) followed by resection of solid tumors for quantifying nuclear shape, KU80 mislocalization, and DNA damage. Anti-KU80 showed approximately threefold higher cytoplasmic immunostaining in shLMNA tumors than Ctl tumors (Fig. 5, B and C). Immunostaining was human specific: mouse nuclei with intense DNA chromocenters showed no anti-KU80 (Fig. 5 B, open arrow). The fraction of shLMNA cells in vivo with mislocalized KU80 was slightly lower than the same cells in vitro on rigid substrates (Fig. 5 D). A549 tumors have a stiffness between that of soft gels and rigid plastic (Swift et al., 2013), which predicts an intermediate rupture level. Lower circularity of shLMNA nuclei in vivo (Fig. 5 D) is consistent with knockdown nuclei being more deformable (Harada et al., 2014). Electrophoretic comet assays showed more DNA damage in shLMNA tumors than Ctl tumors (Fig. 5 E), and in vivo results are again lower than for the same knockdown cells on rigid substrates but are still higher than Ctl's (Fig. 4 C). While additional mechanisms might explain the excess DNA damage, repair factor mislocalization does associate clinically with increased DNA damage (Alshareeda et al., 2016).

In conclusion, nuclear rupture is shown in this study to occur with higher probability at high curvature sites under external probing forces and also under actomyosin forces when cells adhere to stiff ECM (Fig. 5 F). Additional mechanical stress on a strongly curved nucleus might also be important given that curvature does not necessarily equate to either strain or stress in a given structure. Indeed, lamin A behaves in situ as a viscous fluid (Harada et al., 2014), and imposing curvature on a fluid sheet will, over time, dissipate strain and stress, while imposing curvature on a solid sheet (e.g., lamin B in situ) or even lipid bilayers (i.e., liquid crystals) should increase strain, stress, and curvature energy. The latter is useful in understanding breakage of strongly bent microtubules (Odde et al., 1999). Regardless, for medium to high nuclear curvature, lamin A has a protective role under AFM probing (Fig. 1 A) and in adherent cells: in particular, shLMNA and Ctl A549 cells show no significant difference in circularity as a measure of nuclear curvature (Fig. S2 F), and yet nuclear rupture is favored with low lamin A (Fig. 3, A–C; Fig. 4, B and C; and Fig. 5). Nuclear mechanics is complex, but Gaussian curvature (product of two principal surface curvatures at a point) is likely of greater importance than mean curvature because rigid rectangular channels with acute angles cause rupture only in small channels (Denais et al., 2016; Raab et al., 2016). Inward curvature (e.g., AFM poking of Fig. 1) might also differ from outward curvature, but asymmetric plasma membranes with a subsurface cytoskeleton are known to rupture in either case when high forces are rapidly applied to thereby increase membrane tension (Hategan et al., 2003). This is all important to understanding how cell-extrinsic mechanisms such as ECM allow lamin A mutant mice, which typically die in weeks, to achieve a normal lifespan as mosaic mice of 50% normal cells and 50% mutant cells that is sustained in all tissues (de la Rosa et al., 2013). The excess DNA damage quantified in this study indeed shows unusual upstream contributions from ECM rigidity and actomyosin contractility via mechanisms involving curvature-induced lamina rupture and loss of DNA repair factors.

Materials and methods

Cell culture

U2OS human osteosarcoma cells and A549 human lung carcinoma cells were cultured in DMEM high-glucose medium and

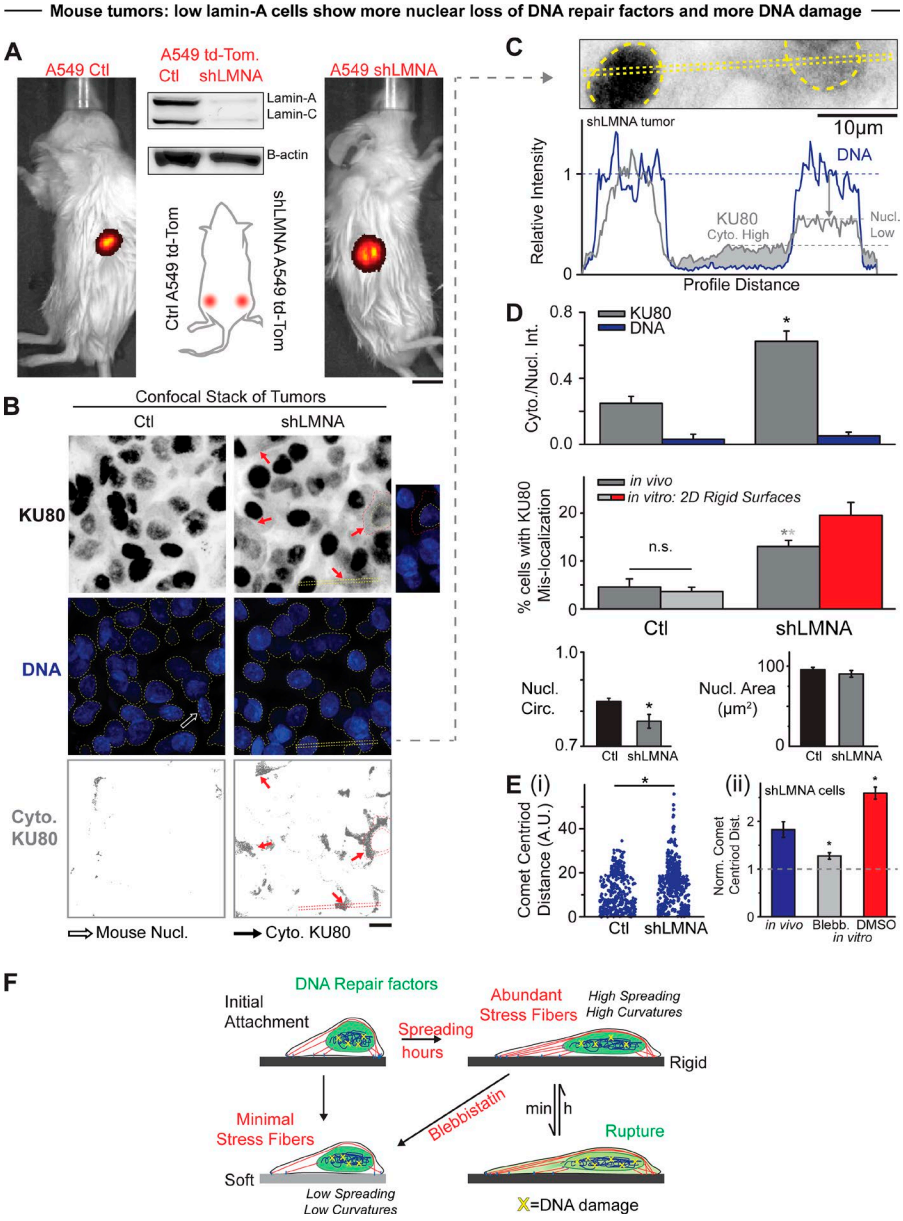

Figure 5. **Solid tumors: Low–lamin A cells show higher curvature nuclei, with increased KU80 mislocalization and DNA damage.** **(A)** A549 Ctl and shLMNA subcutaneous xenografts in NSG mice are monitored by tdTomato fluorescence. Bar, 1 cm. **(B)** Confocal images of A549 Ctl and shLMNA tumors. Red arrows indicate cytoplasmic KU80. The white arrow indicates mouse nucleus with chromocenters. **(C)** Intensity profile of a region of interest in B shows cytoplasmic mislocalization of KU80. **(D)** Top: Cytoplasmic/nuclear KU80 is higher in A549 shLMNA tumors versus Ctl tumors. DNA stain sets baseline for cytoplasm. Middle: Cytoplasmic/nuclear mislocalization in tumors compare well with 2D cultures. Bottom: Nuclear circularity in shLMNA cells is lower than Ctl, while nuclear areas are similar. n = 10 images per tumor from three tumors per group; n > 100 cells for circularity and area. Dark and light gray asterisks indicate significance relative to Ctl. **(E)** Electrophoretic comet assay shows higher DNA damage level in shLMNA tumors compared with Ctl tumors (i) and in vitro shLMNA cultures (ii) treated with blebbistatin but lower than ones treated with DMSO (data from Fig. 4 C). In vitro data are normalized to A549 Ctl cells treated with DMSO. n = 5 tumors. *, P < 0.05. Bars, 10 µm. All data are presented as mean ± SEM. **(F)** Schematic of processes and factors that affect nuclear envelope rupture and excess DNA damage.

Ham's F12 medium (Gibco), respectively, supplemented with 10% FBS and 1% penicillin/streptomycin (MilliporeSigma). Cells were incubated at 37°C and 5% CO_2 as recommended by ATCC. For myosin II inhibition experiments, 20 µM blebbistatin (EMD Millipore) was added to cell culture for 24 h.

Immunostaining

Cells were fixed in 4% formaldehyde (MilliporeSigma) for 15 min followed by 15-min permeabilization by 0.5% Triton X-100 (MilliporeSigma), 30-min blocking by 5% BSA (MilliporeSigma), and overnight incubation in primary antibodies at 4°C. The antibodies used include lamin A/C (1:500; mouse; sc-7292; Santa Cruz Biotechnology, Inc.), lamin A/C (1:500; goat; sc-6215; Santa Cruz Biotechnology, Inc.), lamin B (1:500; goat; sc-6217; Santa Cruz Biotechnology, Inc.), γH2AX (1:500; mouse; 05-636-I; MilliporeSigma), 53BP1 (1:300; rabbit; NB100-304; Novus Biological), KU70 (1:500; mouse; sc-17789; Santa Cruz Biotechnology, Inc.), KU80 (1:500; rabbit; C48E7; Cell Signaling Technology), BRCA1 (1:500; mouse; sc-6954; Santa Cruz Biotechnology, Inc.), BRCA2 (1:500; mouse; sc-293185; Santa Cruz Biotechnology, Inc.), cGAS (1:500; rabbit; D1D3G; Cell Signaling Technology), and collagen I (1:500; mouse; C2456; MilliporeSigma). Finally, after 90 min incubation in secondary antibodies (1:500; donkey anti-mouse, -goat, or -rabbit; Thermo Fisher Scientific), the cells' nuclei were stained with 8 µM Hoechst 33342 (Thermo Fisher Scientific) for 15 min. When used, 1 µg/ml phalloidin-TRITC (MilliporeSigma) was added to cells for 45 min just before Hoechst staining.

Imaging

Conventional epifluorescence images were taken using an Olympus IX71 microscope with a 40×/0.6 NA objective and a digital electron-multiplying charge-coupled device camera (Cascade 512B; Photometrics). Confocal imaging was done on a Leica TCS SP8 system with a 63×/1.4 NA oil-immersion objective.

Live imaging

For live imaging, we used an EVOS FL Auto Imaging System with 10× or 20× object in normal culture conditions (37°C and 5% CO_2; complete culture medium as specified above).

Alkaline comet assay

The assay was performed according to manufacturer instructions (Cell Biolabs). First, cells were detached, mixed with liquefied agarose at 37°C, deposited on a specially treated glass slide, and dried for 15 min at 4°C. Next, the glass slide, containing cells in agarose gel, was incubated in lysis buffer for 45 min and alkaline solution for 30 min. Electrophoresis was conducted at 300 mA for 30 min, and then the slide was washed with 70% ethanol and air dried overnight. Finally, DNA dye was applied for 15 min, and epifluorescence images were taken as described above.

Synthesis of soft and stiff polyacrylamide gels

Round glass coverslips (18 mm; Thermo Fisher Scientific) were cleaned in boiling ethanol and RCA solution (H_2O:H_2O_2:NH_4OH = 2:1:1 in volume) for 10 min each, and then they were functionalized in ATCS solution (chloroform with 0.1% allytrichlorosilane [MilliporeSigma] and 0.1% trimethylamine [MilliporeSigma]) for 1 h. Fresh precursor solution for 0.3-kPa soft gels (3% acrylamide + 0.07% bis-arylamide in deionized water) and 40-kPa stiff gels (10% acrylamide + 0.3% bis-acrylamide in deionized water) were prepared. Then, 0.1% N,N,N′,N′-tetramethylethylenediamine (MilliporeSigma) and 1% ammonium persulphate (MilliporeSigma) were added to each precursor solution, and 20 µl of the resulting mixture was added to each coverslip to allow gel polymerization. To achieve collagen I coating, cross-linker sulfo-SANPAH (50 µg/ml in 50 mM Hepes; G-Biosciences) was applied over the whole gel surface and photoactivated under 365 nm UV light for 7 min. Excess sulfo-SANPAH was washed away following UV activation, and then collagen I solution (100 µg/ml in 50 mM Hepes) was applied overnight at RT with gentle shaking.

Transfection in U2OS cells

All siRNAs used in this study were purchased from GE Healthcare (ON-TARGETplus SMARTpool siBRCA1 L-003461-00, 5′-CAACAUGCCCACAGAUCAA-3′, 5′-CCAAAGCGAGCAAGAGAAU-3′, 5′-UGAUAAAGCUCCAGCAGGA-3′, and 5′-GAAGGAGCUUUCAUCAUUC-3′; siKu80 L-010491-00, 5′-GCAUGGAUGUGAUUCAACA-3′, 5′-CGAGUAACCAGCUCAUAAA-3′, 5′-GAGCAGCGCUUUAACAACU-3′, and 5′-AAACUUCCGUGUUCUAGUG-3′; siLMNA L-004978-00, 5′-GAAGGAGGGUGACCUGAUA-3′, 5′-UCACAGCACGCACGCACUA-3′, 5′-UGAAAGCGCGCAAUACCAA-3′, and 5′-CGUGUGCGCUCGCUGGAAA-3′; and nontargeting siRNA D-001810-10, 5′-UGGUUUACAUGUCGACUAA-3′, 5′-UGGUUUACAUGUUGUGUGA-3′, 5′-UGGUUUACAUGUUUUCUGA-3′, and 5′-UGGUUUACAUGUUUUCCUA-3′), except for si53BP1 (5′-UAUUACCGUCUCCUCGUUC-3′), which was a gift from R. Greenberg (University of Pennsylvania, Philadelphia, PA; Tang et al., 2013). We do not distinguish between lamin A and lamin C because mice seem equally viable expressing either lamin A or lamin C (Fong et al., 2006; Coffinier et al., 2010). GFP-BRCA1 (71116; Addgene) was a gift from D. Durocher (Lunenfeld-Tanenbaum Research Institute, Toronto, Canada); GFP-LBR was a gift from R.-H. Chen (Academia Sinica, Taipei, Taiwan); GFP-KU70 and GFP-KU80 were gifts from S.L. Rulten (University of Sussex, Brighton, UK; Grundy et al., 2013); and GFP-53BP1 and mCherry-cGAS were gifts from R. Greenberg (Harding et al., 2017). GFP-LMNA (Swift et al., 2013), GFP-MIIA, GFP-MIIB, and GFP-MIIA-Y278F were all used in our prior research (Shin et al., 2011). Cells were passaged 24 h before transfection. A complex of siRNA oligonucleotides (25 nM) or GFPs (0.2–0.5 ng/ml) and 1 µg/ml Lipofectamine 2000 (Invitrogen; Thermo Fisher Scientific) was prepared according to the manufacturers' instructions and then added for 3 d (siRNAs) or 24 h (GFPs) to cells in corresponding media supplemented with 10% FBS. GFP-3 in Fig. 4 consists of GFP-KU70, GFP-KU80, and GFP-BRCA1 (0.2–0.5 ng/ml each). All plasmids are confirmed to produce specific functional proteins by Western blotting (Fig. S2) or immunofluorescence (Figs. 1, 2, 3, 4, 5, S2, and S3). Knockdown or overexpression efficiency was determined by immunoblotting or immunofluorescence following standard methods.

Viral transduction

Human LMNA shRNA lentiviral transduction plasmids were purchased from MilliporeSigma (SHCLNG-NM_170707). We transfected these plasmids into bacteria, allowed them to replicate, and then harvested them using a QIAGEN Plasmid Maxi Kit. The resulting purified plasmids were sent to The Wistar Institute (Philadelphia, PA) to produce active lentiviral particles. We then made A549 shLMNA cells according to a standard transduction protocol: ∼1,000,000 cells were seeded in a six-well plate with 2 ml culture medium and then treated for 2 d with active lentiviral particles and 8 µg/ml polybrene (MilliporeSigma). Stable A549 shLMNA clones were generated after puromycin selection. For the LMNA rescue experiments, shLMNA cells were transduced by GFP-LMNA. The LMNA knockdown and rescue efficiency were determined by immunoblotting. Transduction of U2OS was performed according to the same protocol outlined in this study. Unfortunately, shLMNA U2OS cells with low lamin A levels are not stable.

Immunoblotting

For each sample, ∼1,500,000 cells were trypsinized, pelleted, resuspended in 1× LDS lysis buffer supplemented with 1% protease and 1% phosphatase inhibitors, and then sonicated (3 × 15 × 1-s pulses; intermediate power setting). After resting for 30 min on ice, samples were denatured at 80°C with 0.5% β-mercaptoethanol vol/vol for 10 min. Samples were then loaded onto a bis-Tris 4–12% gradient gel (equal loading volumes across all samples; usually 4 µl per 15-well), and electrophoresis was performed (100 V × 10 min; 160 V × 55 min). Finally, proteins were transferred from the gel onto a blotting membrane (iBlot; Thermo Fisher Scientific; settings P3 and 7 min) for antibody staining and detection via standard methods. We used Fiji/ImageJ (National institutes of Health; Schneider et al., 2012) to measure band intensities relative to local background intensities.

Image analysis

Image analysis was typically performed using ImageJ (Schneider et al., 2012). For Fig. 3 C, KU80 mislocalization in ruptured nuclei results in a high cytoplasmic/nuclear ratio based on Fig. 1.

Based on Fig. 2 B, such rupture is 5–10-fold more common for shLMNA cells than either Ctl cells or rescued cells (+GFP-LMNA) that rarely rupture. For the latter, we averaged all data together, whereas for shLMNA cells, we averaged in three bins based on cytoplasmic/nuclear ratio. Bins were defined as either low bin (with similar average and width as Ctl), medium bin (based on width of Ctl), or high bin (the remaining high points). Based on this binning, high KU80 mislocalization correlates with high γH2AX foci counts. Analysis reported in Fig. 5 B (cytoplasmic KU80; bottom) was done in MatLab (MathWorks). To generate the cytoplasmic KU80 images in Fig. 5 B, we uniformly subtracted the KU80 image background intensity from every pixel, and then we removed all signal at the nuclear region, with the bounds of the nucleus determined by Hoechst staining.

Establishment of A549 tumors in vivo

For each injection, ∼1,000,000 cells were suspended in 100 µl ice-cold PBS and 25% Matrigel (BD) and injected subcutaneously into the flank of nonobese diabetic/severe combined immunodeficient mice with null expression of interleukin-2 receptor γ chain (NSG mice). Mice were obtained from the University of Pennsylvania Stem Cell and Xenograft Core. All animal experiments were planned and performed according to Institute of Animal Care and Use Committee protocols.

In vivo tumor imaging

Mice were anesthetized via inhalation of isoflurane at 3 liters/min and maintained at 1.5 liters/min. Images were acquired using a PerkinElmer IVIS Spectrum with excitation and emission filters set at 535 nm and 580 nm, respectively, optimized for tdTomato imaging. Images of each face of the sagittal plane were taken to capture both left and right flanks. Mouse fur was soaked with ethanol to reduce autofluorescence before imaging.

In vitro tumor imaging

Tumors were isolated from mice and fixed in 4% formaldehyde overnight. Fixed samples were then permeabilized by 0.5% Triton X-100 (MilliporeSigma) for 15 min, blocked by 5% BSA (MilliporeSigma) for 30 min, and incubated at 4°C overnight in primary antibodies (listed above in the Immunostaining and Imaging sections). The next day, samples were exposed to secondary antibodies (1:500; Thermo Fisher Scientific) for 90 min, and, finally, were stained with 8 µM Hoechst 33342 (Thermo Fisher Scientific) for 15 min. In taking confocal scans, we excluded the outermost one to two cell layers of each tumor chunk because the peripheral cells are most likely to be physically damaged during sample preparation.

Nuclear indentation by AFM during fluorescent imaging

U2OS cells transfected with various GFP fusion constructs and siLMNA per above or YFP-NLS U2OS were replated on coverslips at a density of 60,000 cells/cm^2 and cultured overnight. Coverslips were mounted in the fluid cell of a hybrid AFM system (MFP-3D-BIO; software: MFP-3D + Igor Pro 6.05; Asylum Research; Oxford Instruments), which has a base plate and X–Y scanner that rest on an inverted optical fluorescence microscope (Olympus IX81 with 40×/0.60 NA objective). Experiments were performed in closed liquid cell at temperature of ∼29°C in DMEM high-glucose medium with 10% serum buffered at pH 7.4 with 25 mM Hepes to prevent cell death in the absence of CO_2 (Frigault et al., 2009). Cells were indented using two types of cantilever probes: (1) MSCT-AUHW (Bruker) cantilevers with nominal spring constant 0.03 N/m, nominal tip radius 10–40 nm, and nominal tip height 2.5–8 µm; and (2) bead probe cantilevers (Novascan) with nominal spring constant 0.06 N/m and a polystyrene beads of 4.5-µm diameter. Before each experiment, cantilever spring constants were calibrated via the thermal fluctuations method to determine indentation forces. Then, a fluorescent cell was chosen for probing by AFM based on expression pattern: for example, expression of GFP in the nucleus without detectable GFP in the cytoplasm even for high exposure times. The cantilever was positioned on the top of the nucleus, and the nucleus was locally compressed with forces of ∼10–30 nN. When the cantilever deflection reached the predefined set point, the tip would dwell on the spot for a predefined time of 100 s before the cantilever was retracted and detached from the cell. Simultaneous fluorescent images were captured every 10 or 15 s for the entire probing cycle, including before force was applied and after the cantilever was retracted for several minutes. In multiple independent experiments that cumulated to 100s of pokes on nuclei inside cells, mCherry-cGAS reliably ruptured in and GFP-KU80 and YFP-NLS cells reliably ruptured out of a major fraction of nuclei (∼50%; Fig. 1, A and B), whereas GFP-53BP1 was less reliable in some experiments for unknown reasons. In addition, when a cell was poked at a position other than the nucleus, plasma membrane rupture was never observed in terms of loss of cytoplasmic fluorescence, while poking over the nucleus rarely showed cytoplasmic rupture (∼1%), consistent with nucleus-specific rupture.

Collagen films self-assembly and AFM imaging

Rat-tail collagen solution (CB354249; Corning; 200 µl at 0.03 mg/ml in 50 mM glycine buffer and 200 mM KCl, pH 9.2) was deposited on freshly cleaved mica disks at room temperature for self-assembly. After 30 min, liquid was gently aspirated, and disks were transferred to Dulbecco's PBS. Collagen films were imaged in PBS at room temperature in tapping mode with NTEGRA (NT-MDT SI), with driving frequencies close to the resonance frequency of cantilevers with a nominal spring constant of 0.1 N/m.

Cell line verification

ATCC is a biological materials resource and standards organization with external accreditation from the International Organization for Standardization, and it provides cell line authentication test recommendations per Tech Bulletin number 8 (TB-0111-00-02; year 2010). This bulletin recommends five types of tests for the authentication of cell lines. (1) Cell morphology check by microscopy, (2) growth curve analysis, and (3) mycoplasma detection by DNA staining (for filaments or extracellular particulates) were conducted on all cell lines used in this study, and all cell lines maintained the expected morphology and standard growth rates with no mycoplasma detected. Two additional ATCC-recommended authentication tests were conducted on the A549 and U2OS cell lines as they were used in all of the main and supplemental

figures. (4) Species verification of A549 cells as human was done by RNA sequencing detection of uniquely human sequences, by mass spectrometry detection of uniquely human sequences, and by antibody targeting with anti-human antibodies. (5) Identity verification from DNA of A549 was confirmed using single nucleotide polymorphism (SNP) arrays (SNPas). DNA was isolated by using the Blood and Cell Culture DNA Mini Kit (QIAGEN) per the manufacturer's instructions, and DNA samples were sent to the Center for Applied Genomics Core in The Children's Hospital of Philadelphia (Philadelphia, PA) for the SNPa HumanOmniExpress-24 Bead Chip Kit (Illumina), with >700,000 probes along the entire human genome. For each sample, the Genomics Core provided the data in the form of GenomeStudio files (Illumina). Chromosome copy number was analyzed in GenomeStudio with the cnvPartition plugin (Illumina). SNPa experiments also provided genotype data, which was used to give single nucleotide variant data. Genotyping in this Illumina system relied on the correlation between total intensity and intensity ratio of the two probes, one for CG and another for AT. These correlations were mapped to a standard clustering file (Illumina) to give the SNP calls. Consistent with ATCC's karyotype analysis, SNPa showed that the A549 cells are hypotriploid with a chromosome copy number of 66, including two copies of X and Y chromosomes and four copies of chromosome 17. Further consistent with ATCC's descriptions of this cell line as Caucasian in origin, SNPa analyses show that the A549 cells are mostly European in ancestry (~90%; Dodecad2.1 an ancestry lineage algorithm that has used mostly Illumina SNPa data; Alvey et al., 2017). Similarly, U2OS cells used in our laboratory contained ~65 chromosomes by SNPa analysis, consistent with altered chromosomes reported by ATCC, and genomic drift in terms of copy number variation was low during standard culture as clonality of U2OS cells can be maintained after single-cell cloning and continuous culture for months (Irianto et al., 2017).

Determining nuclear envelope rupture

The ratio of a protein's total cytoplasmic intensity to its total nuclear intensity (i.e., cytoplasmic/nuclear ratio) in immunofluorescence images of fixed cells is determined by the abundance of that particular protein as well as by antibody specificity. As a result, anti-53BP1 and anti-KU80 can generate different cytoplasmic/nuclear ratio values for nonruptured nuclei in images. Based on confocal images of anti-KU80, nonruptured nuclei have a cytoplasmic/nuclear ratio of <0.1 (Irianto et al., 2017). To confirm this finding and validate the cytoplasmic/nuclear ratio as an indicator of rupture, we validated with the cells in Fig. S1 E. As shown, when the cytoplasmic/nuclear ratio is >0.1, the nuclear intensity of KU80 is low compared with nearby cells, and KU80 fills the cytoplasm and becomes visible (Fig. S1 E, arrows). Thus, the cytoplasmic/nuclear ratio reflects rupture-induced changes in protein localization, providing confidence in this ratio as a method to detect nuclear envelope rupture. To be clear, all cytoplasmic/nuclear signal used in this study is the ratio of integrated intensity in the cytoplasm over integrated intensity in the nucleus.

High, medium, or low curvature

Constricted migration through 3-µm pores causes nuclear envelope rupture in most U2OS cells, whereas 8-µm pores cause nuclear rupture in only a small fraction of cells (Irianto et al., 2017). We therefore describe AFM probes <3 µm in diameter to be high curvature, 3–7 µm to be medium curvature, and >8 µm to be low curvature.

GFP-3 rescue experiment in Fig. 4 A

U2OS siLMNA cells were plated on rigid plastic and cultured overnight, and then they were transfected with either GFP-3 (consisting of GFP-KU70, GFP-KU80, and GFP-BRCA1) or GFP-53BP1. A third Ctl sample was not transfected; we refer to these cells as nontreated (NT). After a 24-h transfection period, all cells were fixed and immunostained for γH2AX, and the NT sample was additionally immunostained for KU80. Cytoplasmic GFP signal (or KU80 signal in the NT case) was used to identify ruptured nuclei. Foci of γH2AX were counted for ruptured and nonruptured nuclei in all three samples.

Determining pole and side regions of nuclei

ImageJ was used to first fit an ellipse for a certain nucleus, and then the ellipse was split into three regions such that the total area of the two pole regions was approximately the same as the midbody region. For ruptured nuclei, the lamin A disruption on the nuclear envelope resided in either a pole region or the side, midbody region.

Circularity, curvature, and ellipse theory

Circularity describes how the shape varies from a circle. It is a property of the entire shape and is dimensionless (i.e., it does not depend on the size of the shape):

$$C = \frac{4\pi A}{P^2}, \tag{1}$$

where A is the area and P is the perimeter.

Curvature can vary around the boundary of a shape and has dimensions of 1/length:

$$\kappa = \frac{1}{R}, \tag{2}$$

where R is the radius of curvature at any given point on the curve. To compare variation in curvature and dimensionless circularity, we will use the curvature of a circle with the same area to normalize variation in curvature.

Let's restrict our considerations to ellipses. We define an ellipse parametrically as

$$x(t) = a^*\cos(t),\ y(t) = b^*\sin(t), \tag{3}$$

where a is the semimajor axis and b is the semiminor axis.

Circularity of an ellipse

The area of an ellipse is

$$A_{ellipse} = \pi ab, \tag{4}$$

and the perimeter of an ellipse is given by an elliptic integral is

$$P_{ellipse} = \int_0^{2\pi} dt\sqrt{a^2 sin^2 t + b^2 cos^2 t}. \tag{5}$$

Ramanujan's approximation to the perimeter is

$$P_{Ram} = \pi(a+b)\left(1+\frac{3\lambda}{10+\sqrt{4-3\lambda}}\right),\ \lambda = \frac{\left(1-\frac{b}{a}\right)^2}{\left(1+\frac{b}{a}\right)^2}, \quad (6)$$

so the circularity of an ellipse can be approximated as

$$C_{ellipse} \approx \frac{4ab}{\left(a+b\right)^2\left(1+\frac{3\lambda}{10+\sqrt{4-3\lambda}}\right)^2}, \quad (7)$$

or in terms of the ratio of the minor and major semiaxes, $r = a/b$,

$$C_{ellipse} \approx \frac{4ab}{\left(r+2+\frac{1}{r}\right)^2\left(1+\frac{3\lambda}{10+\sqrt{4-3\lambda}}\right)^2},$$
$$\lambda = \frac{\left(1-\frac{1}{r}\right)^2}{\left(1+\frac{1}{r}\right)^2}. \quad (8)$$

Curvature of an ellipse

The curvature of an ellipse defined by Eq. 3 is

$$\kappa_{ellipse} = \frac{ab}{(a^2sin^2t + b^2cos^2t)^{3/2}}. \quad (9)$$

The maximum curvature is

$$\kappa_{max} = \frac{a}{b^2} \quad (10)$$

(where we have assumed without loss of generality that $a > b > 0$). The curvature of a circle with the same area as the ellipse defined by Eq. 3 is

$$\kappa_{circle} = \frac{1}{\sqrt{ab}}. \quad (11)$$

Let's use $\kappa_{norm} = (\kappa_{max})/\kappa_{circle}$ as a normalized measure of the range in curvature. In terms of $r = b/a$, we have

$$\kappa_{norm} = r^{\frac{3}{2}}. \quad (12)$$

Measured normalized maximum curvature

ImageJ was used to mark the contour of a nucleus, and then we drew a circle of radius R to be tangent to the pole of the nucleus with highest curvature. This gives the maximum curvature

$$\kappa = \frac{1}{R},$$

and a few nuclei ($n > 3$) were also analyzed using the ImageJ plugin "kappa curvature analysis" to confirm consistency with our fitted circle approach. We normalized by

$$\kappa_{circle} = \frac{1}{R} = 1/\sqrt{A/\pi},$$

where r is the radius of the circle with the same area as the nucleus and A is the area of the nucleus measured by ImageJ. Thus, $\kappa_{norm} = \kappa/\kappa_{circle}$.

Statistical analyses

All statistical analyses were performed using Excel (2013; Microsoft). Unless otherwise noted, statistical comparisons were made by unpaired two-tailed Student's *t* tests and were considered significant if $P < 0.05$. Unless mentioned, all plots show mean ± SEM. *n* indicates the number of samples, cells, or wells quantified in each experiment. Figure legends specify the exact meaning of *n* for each figure (Cumming et al., 2007). For figures presenting pooled data (Fig. 5 E), all numbers are normalized to Ctl cells that do not show variations across experiments followed by unpaired two-tailed Student's *t* tests.

Online supplemental material

Fig. S1 shows how lamin A knockdown can affect cell growth as well as sustained but rapid mislocalization of multiple repair factors (unlike YFP-NLS) and DNA damage. Fig. S2 shows how many repair factors mislocalize, how their partial knockdown increases DNA damage, and how actomyosin inhibition favors rapid nuclear rounding without affecting repair factor levels. Fig. S3 shows how increased actomyosin stress can increase nuclear curvature as well as frequency of nuclear envelope rupture and DNA damage without affecting cell cycle.

Acknowledgments

The authors would like to thank Dr. Stuart L. Rulten for various DNA damage response protein plasmids used in this study.

The authors in this study were supported by the National Institutes of Health National Cancer Institute under Physical Sciences Oncology Center Award U54 CA193417, Human Frontiers Sciences Program grant RGP0024, National Heart, Lung, and Blood Institute award R21 HL128187, the US–Israel Binational Science Foundation, National Science Foundation grant agreement CMMI 15-48571, and the Simons Foundation (327939). This content is solely the responsibility of the authors and does not necessarily represent the official views of the National Institutes of Health nor the National Science Foundation.

The authors declare no competing financial interests.

Author contributions: Y. Xia, I.L. Ivanovksa, and D.E. Discher designed experiments. A.J. Liu and R.A. Greenberg contributed key materials, methods, and discussion. Y. Xia, I.L. Ivanovska, K. Zhu, L. Smith, C.M. Alvey, J. Irianto, C.R. Pfeifer, S. Cho, J. Ji, A.J. Liu, S. Cho, and R.R. Bennett performed and analyzed experiments. Y. Xia, I.L. Ivanovska, and D.E. Discher wrote the manuscript.

Submitted: 8 December 2017
Revised: 24 May 2018
Accepted: 20 August 2018

References

Alshareeda, A.T., O.H. Negm, M.A. Aleskandarany, A.R. Green, C. Nolan, P.J. TigHhe, S. Madhusudan, I.O. Ellis, and E.A. Rakha. 2016. Clinical and biological significance of RAD51 expression in breast cancer: a key DNA damage response protein. *Breast Cancer Res. Treat.* 159:41–53. https://doi.org/10.1007/s10549-016-3915-8

Álvarez-Quilón, A., A. Serrano-Benítez, J.A. Lieberman, C. Quintero, D. Sánchez-Gutiérrez, L.M. Escudero, and F. Cortés-Ledesma. 2014. ATM specifically mediates repair of double-strand breaks with blocked DNA ends. *Nat. Commun.* 5:3347. https://doi.org/10.1038/ncomms4347

Alvey, C.M., K.R. Spinler, J. Irianto, C.R. Pfeifer, B. Hayes, Y. Xia, S. Cho, P. Dingal, J. Hsu, L. Smith, et al. 2017. SIRPA-Inhibited, Marrow-Derived Macrophages Engorge, Accumulate, and Differentiate in Antibody-Targeted Regression of Solid Tumors. *Curr. Biol.* 27:2065–2077.

Broers, J.L., Y. Raymond, M.K. Rot, H. Kuijpers, S.S. Wagenaar, and F.C. Ramaekers. 1993. Nuclear A-type lamins are differentially expressed in human lung cancer subtypes. *Am. J. Pathol.* 143:211–220.

Burma, S., B.P. Chen, M. Murphy, A. Kurimasa, and D.J. Chen. 2001. ATM phosphorylates histone H2AX in response to DNA double-strand breaks. *J. Biol. Chem.* 276:42462–42467. https://doi.org/10.1074/jbc.C100466200

Buxboim, A., J. Swift, J. Irianto, K.R. Spinler, P.C. Dingal, A. Athirasala, Y.R. Kao, S. Cho, T. Harada, J.W. Shin, and D.E. Discher. 2014. Matrix elasticity regulates lamin-A,C phosphorylation and turnover with feedback to actomyosin. *Curr. Biol.* 24:1909–1917. https://doi.org/10.1016/j.cub.2014.07.001

Buxboim, A., J. Irianto, J. Swift, A. Athirasala, J.W. Shin, F. Rehfeldt, and D.E. Discher. 2017. Coordinated increase of nuclear tension and lamin-A with matrix stiffness outcompetes lamin-B receptor that favors soft tissue phenotypes. *Mol. Biol. Cell.* 28:3333–3348. https://doi.org/10.1091/mbc.e17-06-0393

Capo-chichi, C.D., K.Q. Cai, J. Smedberg, P. Ganjei-Azar, A.K. Godwin, and X.X. Xu. 2011. Loss of A-type lamin expression compromises nuclear envelope integrity in breast cancer. *Chin. J. Cancer.* 30:415–425. https://doi.org/10.5732/cjc.010.10566

Chang, H.H.Y., N.R. Pannunzio, N. Adachi, and M.R. Lieber. 2017. Non-homologous DNA end joining and alternative pathways to double-strand break repair. *Nat. Rev. Mol. Cell Biol.* 18:495–506. https://doi.org/10.1038/nrm.2017.48

Coffinier, C., H.J. Jung, Z. Li, C. Nobumori, U.J. Yun, E.A. Farber, B.S. Davies, M.M. Weinstein, S.H. Yang, J. Lammerding, et al. 2010. Direct synthesis of lamin A, bypassing prelamin a processing, causes misshapen nuclei in fibroblasts but no detectable pathology in mice. *J. Biol. Chem.* 285:20818–20826. https://doi.org/10.1074/jbc.M110.128835

Cumming, G., F. Fidler, and D.L. Vaux. 2007. Error bars in experimental biology. *J. Cell Biol.* 177:7–11. https://doi.org/10.1083/jcb.200611141

Darzynkiewicz, Z., H.D. Halicka, H. Zhao, and M. Podhorecka. 2011. Cell synchronization by inhibitors of DNA replication induces replication stress and DNA damage response: analysis by flow cytometry. *Methods Mol. Biol.* 761:85–96. https://doi.org/10.1007/978-1-61779-182-6_6

Das, A., D.A. Grotsky, M.A. Neumann, R. Kreienkamp, I. Gonzalez-Suarez, A.B. Redwood, B.K. Kennedy, C.L. Stewart, and S. Gonzalo. 2013. Lamin A Δexon9 mutation leads to telomere and chromatin defects but not genomic instability. *Nucleus.* 4:410–419. https://doi.org/10.4161/nucl.26873

de la Rosa, J., J.M. Freije, R. Cabanillas, F.G. Osorio, M.F. Fraga, M.S. Fernández-García, R. Rad, V. Fanjul, A.P. Ugalde, Q. Liang, et al. 2013. Prelamin A causes progeria through cell-extrinsic mechanisms and prevents cancer invasion. *Nat. Commun.* 4:2268. https://doi.org/10.1038/ncomms3268

Denais, C.M., R.M. Gilbert, P. Isermann, A.L. McGregor, M. te Lindert, B. Weigelin, P.M. Davidson, P. Friedl, K. Wolf, and J. Lammerding. 2016. Nuclear envelope rupture and repair during cancer cell migration. *Science.* 352:353–358. https://doi.org/10.1126/science.aad7297

De Vos, W.H., F. Houben, M. Kamps, A. Malhas, F. Verheyen, J. Cox, E.M. Manders, V.L. Verstraeten, M.A. van Steensel, C.L. Marcelis, et al. 2011. Repetitive disruptions of the nuclear envelope invoke temporary loss of cellular compartmentalization in laminopathies. *Hum. Mol. Genet.* 20:4175–4186. https://doi.org/10.1093/hmg/ddr344

Dingal, P.C., A.M. Bradshaw, S. Cho, M. Raab, A. Buxboim, J. Swift, and D.E. Discher. 2015. Fractal heterogeneity in minimal matrix models of scars modulates stiff-niche stem-cell responses via nuclear exit of a mechanorepressor. *Nat. Mater.* 14:951–960. https://doi.org/10.1038/nmat4350

Docheva, D., E.B. Hunziker, R. Fässler, and O. Brandau. 2005. Tenomodulin is necessary for tenocyte proliferation and tendon maturation. *Mol. Cell. Biol.* 25:699–705. https://doi.org/10.1128/MCB.25.2.699-705.2005

Elosegui-Artola, A., I. Andreu, A.E.M. Beedle, A. Lezamiz, M. Uroz, A.J. Kosmalska, R. Oria, J.Z. Kechagia, P. Rico-Lastres, A.L. Le Roux, et al. 2017. Force Triggers YAP Nuclear Entry by Regulating Transport across Nuclear Pores. *Cell.* 171:1397–1410. https://doi.org/10.1016/j.cell.2017.10.008

Fong, L.G., J.K. Ng, J. Lammerding, T.A. Vickers, M. Meta, N. Coté, B. Gavino, X. Qiao, S.Y. Chang, S.R. Young, et al. 2006. Prelamin A and lamin A appear to be dispensable in the nuclear lamina. *J. Clin. Invest.* 116:743–752. https://doi.org/10.1172/JCI27125

Frigault, M.M., J. Lacoste, J.L. Swift, and C.M. Brown. 2009. Live-cell microscopy - tips and tools. *J. Cell Sci.* 122:753–767. https://doi.org/10.1242/jcs.033837

Grundy, G.J., S.L. Rulten, Z. Zeng, R. Arribas-Bosacoma, N. Iles, K. Manley, A. Oliver, and K.W. Caldecott. 2013. APLF promotes the assembly and activity of non-homologous end joining protein complexes. *EMBO J.* 32:112–125. https://doi.org/10.1038/emboj.2012.304

Gudmundsdottir, K., and A. Ashworth. 2006. The roles of BRCA1 and BRCA2 and associated proteins in the maintenance of genomic stability. *Oncogene.* 25:5864–5874. https://doi.org/10.1038/sj.onc.1209874

Harada, T., J. Swift, J. Irianto, J.W. Shin, K.R. Spinler, A. Athirasala, R. Diegmiller, P.C. Dingal, I.L. Ivanovska, and D.E. Discher. 2014. Nuclear lamin stiffness is a barrier to 3D migration, but softness can limit survival. *J. Cell Biol.* 204:669–682. https://doi.org/10.1083/jcb.201308029

Harding, S.M., J.L. Benci, J. Irianto, D.E. Discher, A.J. Minn, and R.A. Greenberg. 2017. Mitotic progression following DNA damage enables pattern recognition within micronuclei. *Nature.* 548:466–470. https://doi.org/10.1038/nature23470

Hatch, E.M., and M.W. Hetzer. 2016. Nuclear envelope rupture is induced by actin-based nucleus confinement. *J. Cell Biol.* 215:27–36. https://doi.org/10.1083/jcb.201603053

Hategan, A., R. Law, S. Kahn, and D.E. Discher. 2003. Adhesively-tensed cell membranes: lysis kinetics and atomic force microscopy probing. *Biophys. J.* 85:2746–2759. https://doi.org/10.1016/S0006-3495(03)74697-9

Hernandez, L., K.J. Roux, E.S. Wong, L.C. Mounkes, R. Mutalif, R. Navasankari, B. Rai, S. Cool, J.W. Jeong, H. Wang, et al. 2010. Functional coupling between the extracellular matrix and nuclear lamina by Wnt signaling in progeria. *Dev. Cell.* 19:413–425. https://doi.org/10.1016/j.devcel.2010.08.013

Irianto, J., Y. Xia, C.R. Pfeifer, A. Athirasala, J. Ji, C. Alvey, M. Tewari, R.R. Bennett, S.M. Harding, A.J. Liu, et al. 2017. DNA Damage Follows Repair Factor Depletion and Portends Genome Variation in Cancer Cells after Pore Migration. *Curr. Biol.* 27:210–223. https://doi.org/10.1016/j.cub.2016.11.049

Ivanovska, I.L., J. Swift, K. Spinler, D. Dingal, S. Cho, and D.E. Discher. 2017. Cross-linked matrix rigidity and soluble retinoids synergize in nuclear lamina regulation of stem cell differentiation. *Mol. Biol. Cell.* 28:2010–2022. https://doi.org/10.1091/mbc.e17-01-0010

Kaspi, E., D. Frankel, J. Guinde, S. Perrin, S. Laroumagne, A. Robaglia-Schlupp, K. Ostacolo, K. Harhouri, R. Tazi-Mezalek, J. Micallef, et al. 2017. Low lamin A expression in lung adenocarcinoma cells from pleural effusions is a pejorative factor associated with high number of metastatic sites and poor Performance status. *PLoS One.* 12:e0183136. https://doi.org/10.1371/journal.pone.0183136

Lammerding, J., K.N. Dahl, D.E. Discher, and R.D. Kamm. 2007. Nuclear mechanics and methods. *Methods Cell Biol.* 83:269–294. https://doi.org/10.1016/S0091-679X(07)83011-1

Larrieu, D., S. Britton, M. Demir, R. Rodriguez, and S.P. Jackson. 2014. Chemical inhibition of NAT10 corrects defects of laminopathic cells. *Science.* 344:527–532. https://doi.org/10.1126/science.1252651

Levental, K.R., H. Yu, L. Kass, J.N. Lakins, M. Egeblad, J.T. Erler, S.F. Fong, K. Csiszar, A. Giaccia, W. Weninger, et al. 2009. Matrix crosslinking forces tumor progression by enhancing integrin signaling. *Cell.* 139:891–906. https://doi.org/10.1016/j.cell.2009.10.027

Nuciforo, P.G., C. Luise, M. Capra, G. Pelosi, and F. d'Adda di Fagagna. 2007. Complex engagement of DNA damage response pathways in human cancer and in lung tumor progression. *Carcinogenesis.* 28:2082–2088. https://doi.org/10.1093/carcin/bgm108

Odde, D.J., L. Ma, A.H. Briggs, A. DeMarco, and M.W. Kirschner. 1999. Microtubule bending and breaking in living fibroblast cells. *J. Cell Sci.* 112:3283–3288.

Oh, T.I., Y.M. Lee, B.O. Lim, and J.H. Lim. 2017. Inhibition of NAT10 Suppresses Melanogenesis and Melanoma Growth by Attenuating Microphthalmia-Associated Transcription Factor (MITF) Expression. *Int. J. Mol. Sci.* 18:1924. https://doi.org/10.3390/ijms18091924

Raab, M., M. Gentili, H. de Belly, H.R. Thiam, P. Vargas, A.J. Jimenez, F. Lautenschlaeger, R. Voituriez, A.M. Lennon-Duménil, N. Manel, and M. Piel. 2016. ESCRT III repairs nuclear envelope ruptures during cell migration to limit DNA damage and cell death. *Science.* 352:359–362. https://doi.org/10.1126/science.aad7611

Saez, A., A. Buguin, P. Silberzan, and B. Ladoux. 2005. Is the mechanical activity of epithelial cells controlled by deformations or forces? *Biophys. J.* 89:L52–L54. https://doi.org/10.1529/biophysj.105.071217

Samudram, A., B.M. Mangalassery, M. Kowshik, N. Patincharath, and G.K. Varier. 2016. Passive permeability and effective pore size of HeLa cell nuclear membranes. *Cell Biol. Int.* 40:991–998. https://doi.org/10.1002/cbin.10640

Schneider, C.A., W.S. Rasband, and K.W. Eliceiri. 2012. NIH Image to ImageJ: 25 years of image analysis. *Nat. Methods.* 9:671–675. https://doi.org/10.1038/nmeth.2089

Seluanov, A., J. Danek, N. Hause, and V. Gorbunova. 2007. Changes in the level and distribution of Ku proteins during cellular senescence. *DNA Repair (Amst.).* 6:1740–1748. https://doi.org/10.1016/j.dnarep.2007.06.010

Shin, J.W., J. Swift, K.R. Spinler, and D.E. Discher. 2011. Myosin-II inhibition and soft 2D matrix maximize multinucleation and cellular projections typical of platelet-producing megakaryocytes. *Proc. Natl. Acad. Sci. USA.* 108:11458–11463. https://doi.org/10.1073/pnas.1017474108

Soubeyrand, S., L. Pope, and R.J. Haché. 2010. Topoisomerase IIalpha-dependent induction of a persistent DNA damage response in response to transient etoposide exposure. *Mol. Oncol.* 4:38–51. https://doi.org/10.1016/j.molonc.2009.09.003

Staszewski, O., T. Nikolova, and B. Kaina. 2008. Kinetics of gamma-H2AX focus formation upon treatment of cells with UV light and alkylating agents. *Environ. Mol. Mutagen.* 49:734–740. https://doi.org/10.1002/em.20430

Swift, J., I.L. Ivanovska, A. Buxboim, T. Harada, P.C. Dingal, J. Pinter, J.D. Pajerowski, K.R. Spinler, J.W. Shin, M. Tewari, et al. 2013. Nuclear lamin-A scales with tissue stiffness and enhances matrix-directed differentiation. *Science.* 341:1240104. https://doi.org/10.1126/science.1240104

Takaki, T., M. Montagner, M.P. Serres, M. Le Berre, M. Russell, L. Collinson, K. Szuhai, M. Howell, S.J. Boulton, E. Sahai, and M. Petronczki. 2017. Actomyosin drives cancer cell nuclear dysmorphia and threatens genome stability. *Nat. Commun.* 8:16013. https://doi.org/10.1038/ncomms16013

Tamiello, C., M.A. Kamps, A. van den Wijngaard, V.L. Verstraeten, F.P. Baaijens, J.L. Broers, and C.C. Bouten. 2013. Soft substrates normalize nuclear morphology and prevent nuclear rupture in fibroblasts from a laminopathy patient with compound heterozygous LMNA mutations. *Nucleus.* 4:61–73. https://doi.org/10.4161/nucl.23388

Tang, J., N.W. Cho, G. Cui, E.M. Manion, N.M. Shanbhag, M.V. Botuyan, G. Mer, and R.A. Greenberg. 2013. Acetylation limits 53BP1 association with damaged chromatin to promote homologous recombination. *Nat. Struct. Mol. Biol.* 20:317–325. https://doi.org/10.1038/nsmb.2499

Turgay, Y., M. Eibauer, A.E. Goldman, T. Shimi, M. Khayat, K. Ben-Harush, A. Dubrovsky-Gaupp, K.T. Sapra, R.D. Goldman, and O. Medalia. 2017. The molecular architecture of lamins in somatic cells. *Nature.* 543:261–264. https://doi.org/10.1038/nature21382

Wang, N., J.D. Tytell, and D.E. Ingber. 2009. Mechanotransduction at a distance: mechanically coupling the extracellular matrix with the nucleus. *Nat. Rev. Mol. Cell Biol.* 10:75–82. https://doi.org/10.1038/nrm2594